crystals

MDPI

Article

Microstructure Analysis and Thermoelectric Properties of Melt-Spun Bi-Sb-Te Compounds

Weon Ho Shin [1], Jeong Seop Yoon [1], Mahn Jeong [1], Jae Min Song [1], Seyun Kim [2], Jong Wook Roh [2], Soonil Lee [1], Won Seon Seo [1], Sung Wng Kim [3,*] and Kyu Hyoung Lee [4,*]

1 Energy Materials Center, Energy & Environment Division, Korea Institute of Ceramic Engineering & Technology, Jinju 52851, Korea; whshin@kicet.re.kr (W.H.S.); yujsyoon@kicet.re.kr (J.S.Y.), sensjm@kicet.re.kr (M.J.); love8767@kicet.re.kr (J.M.S.); silee@kicet.re.kr (S.L.); wsseo@kicet.re.kr (W.S.S.)
2 Materials R & D Center, Samsung Advanced Institute of Technology, Samsung Electronics, Suwon 16419, Korea; seyuni.kim@samsung.com (S.K.); jw.roh@samsung.com (J.W.R.)
3 Department of Energy Science, Sungkyunkwan University, Suwon 16419, Korea
4 Department of Nano Applied Engineering, Kangwon National University, Chuncheon 24341, Korea
* Correspondence: kimsungwng@skku.edu (S.W.K.); khlee2014@kangwon.ac.kr (K.H.L.); Tel.: +82-31-299-6274 (S.W.K.); +82-33-250-6261 (K.H.L.)

Academic Editor: George S. Nolas
Received: 25 May 2017; Accepted: 19 June 2017; Published: 20 June 2017

Abstract: In order to realize high-performance thermoelectric materials, a way to obtain small grain size is necessary for intensification of the phonon scattering. Here, we use a melt-spinning-spark plasma sintering process for making p-type $Bi_{0.36}Sb_{1.64}Te_3$ thermoelectric materials and evaluate the relation between the process conditions and thermoelectric performance. We vary the Cu wheel rotation speed from 1000 rpm (~13 ms^{-1}) to 4000 rpm (~52 ms^{-1}) during the melt spinning process to change the cooling rate, allowing us to control the characteristic size of nanostructure in melt-spun $Bi_{0.36}Sb_{1.64}Te_3$ ribbons. The higher wheel rotation speed decreases the size of nanostructure, but the grain sizes of sintered pellets are inversely proportional to the nanostructure size after the same sintering condition. As a result, the ZT values of the bulks fabricated from 1000–3000 rpm melt-spun ribbons are comparable each other, while the ZT value of the bulk from the 4000 rpm melt-spun ribbons is rather lower due to reduction of grain boundary phonon scattering. In this work, we can conclude that the smaller nanostructure in the melt spinning process does not always guarantee high-performance thermoelectric bulks, and an adequate following sintering process must be included.

Keywords: thermoelectric; phonon scattering; melt spinning; $Bi_{0.36}Sb_{1.64}Te_3$; nanostructure

1. Introduction

The increasing world-wide demands on new technology for CO_2 reduction and global warming have induced the development of highly-efficient energy harvesting technology that reuses exhausted energy and shifts from fossil fuels to renewable energy and replaces it with new energy sources. Currently, more than 60% of primary energy used in industry or in combustion engines is lost as waste heat. Thermoelectricity is considered to be one of the encouraging energy harvesting technologies in the view of changing waste heat into electricity in the semiconductor materials [1,2]. The efficiency of thermoelectric (TE) devices is highly related with the performance of TE materials, which is determined by a dimensionless figure of merit, ZT, calculated by $ZT = \sigma S^2 T/\kappa$, where σ, S, T, and κ are the electrical conductivity, Seebeck coefficient, absolute temperature, and thermal conductivity, respectively [3,4]. High σ, high S, and low κ are essential to make high-performance TE materials; however, these

transport parameters are correlated with each other in terms of carrier concentration, practically limiting to the ZT value of ~1.

Bi_2Te_3-based alloys are considered to be the best TE materials for near room temperature [5,6], and are the only commercialized materials applied for TE cooling and low-temperature power generation applications; however, they are still limited in special fields due to a low TE performance [7,8]. In order to design high TE materials, two different approaches are proposed: (1) enhancing power factor (PF = σS^2) and (2) reducing κ. The κ is divided by two terms of electronic contribution (κ_{ele}) and lattice contribution ($\kappa_{lat} = \kappa - \kappa_{ele}$). The κ_{ele} is in proportion to σ according to the Wiedemann–Franz law $\kappa_{ele} = L\sigma T$, where L is the Lorenz number [9]. In this context, many researchers are focusing on the κ_{lat} reduction which is considered as an independent variable to enhance TE performance [1,8,10,11]. Recent studies have shown a significant reduction of κ_{lat} with integrated defects, resulting in high ZT values for various TE materials [8,12–14]. However, these technologies are still far from commercialization in terms of mass production. The continuous attempts to reduce grain size of the TE materials have been tried via high-energy ball milling [15,16], spark erosion [17], melt spinning (MS) [8,18–20], and bottom-up chemical synthesis processes [21–23].

According to several reports [8,18–20], the MS process is proven to be effective for the realization of nano-scale sized Bi_2Te_3-based TE materials. However, it is necessary to investigate the process variables, leading to different microstructures and transport properties which are critical factors for TE performance. Adjusting the wheel rotation speed during the MS process can induce the variation of thickness and microstructure of melt-spun ribbons, which control the TE performance of their bulks with the same composition. In the present work, we have investigated the change of microstructure and TE properties of polycrystalline bulks of $Bi_{0.36}Sb_{1.64}Te_3$ fabricated by combined technique of MS and spark plasma sintering (SPS) in an effort to optimize the process parameters for nanograin structured TE materials.

2. Experimental Details

High purity elemental Bi (99.999%, 5N Plus), Sb (99.999%, 5N Plus), and Te (99.999%, 5N Plus) granules as starting materials were weighed according to the formula of $Bi_{0.36}Sb_{1.64}Te_3$. Excess 1 wt % Te was added due to Te evaporation. The raw materials were loaded into a vacuum-sealed quartz ampule and then melted at 1373 K for 4 h. The obtained ingots were pulverized, and the powders were compacted by a hydraulic press. The compactions were put into a graphite nozzle with 0.4 mm diameter. The MS process was used for the fabrication of nanostructured ribbons of $Bi_{0.36}Sb_{1.64}Te_3$. The Cu wheel (diameter ~250 mm) rotation speeds were varied as 1000 rpm (~13.1 ms^{-1}), 2000 rpm (~26.2 ms^{-1}), 3000 rpm (~39.3 ms^{-1}), and 4000 rpm (~52.4 ms^{-1}). Thin ribbons were produced by MS process, and the ribbons show amorphous structure on the contact surface and crystalline nanostructure on the free surface. The melt-spun ribbons were pulverized into powders and sintered using SPS at 753 K for 3 min under 60 MPa. The dimension of SPSed pellets is in the diameter of 12.5 mm and the height of 10 mm in this work.

X-ray diffraction (XRD, New D8 Advance, Bruker, Cu Kα) for SPSed pellets was performed on parallel and perpendicular planes of SPS pressing direction. The microstructure was investigated using scanning electron microscopy (SEM) (JSM-7600F, JEOL, Peabody, MA, USA). The temperature dependences of the σ and S were measured from room temperature to 473 K by a four-point probe method using the ZEM-3 apparatus (ULVAC-RIKO). Carrier concentrations and mobilities were obtained from Hall effect measurement system (HT-Hall, ResiTest 8300, Toyo Corporation, Toyo, Japan). The κ values were measured by laser-flash analysis (LFA) using TA Netzsch LFA 457. All measured TE transport data were acquired at the same dimension and configuration, and were obtained within the experimental error of σ (~4%), S (~4%), and κ (~5%). Thus, we assume total uncertainty of ZT as ~12%.

3. Results and Discussion

3.1. Microstructure Analysis

After the MS process, we can obtain thin and short (~2 mm in width and ~10 mm in length) ribbon-shaped materials with an amorphous structure on the contact surface and nano-scale structure on the free surface [20]. The Cu wheel rotation speed during the MS process would be a major factor determining the cooling rate. Figure 1 shows the SEM images of the cross-section of melt-spun $Bi_{0.36}Sb_{1.56}Te_3$ ribbons with varying wheel rotation speeds of 1000 rpm, 2000 rpm, and 4000 rpm. As shown in Figure 1, increasing wheel rotation speed from 1000 rpm to 4000 rpm results in a decrease of the ribbon thickness from 17.8 μm to 3.38 μm. The thickness is inversely proportional with the wheel rotation speed, which is in good agreement with the previous reports [24,25], and the melt-spun ribbon is composed of non-crystalline contact surface and crystalline free surface [20]. The nanostructure of the free surface also changes with the wheel rotation speed, as shown in Figure 2. The thickness of rod-shaped nanograin decreased with increasing wheel rotation speed: 503 nm for 1000 rpm, 451 nm for 2000 rpm, and 372 nm for 4000 rpm, respectively, averaged by more than 20 batches of melt-spun ribbons. It is also noteworthy that the pore sizes among nanostructures were smaller as the wheel rotation speed increased, caused by higher growth rate. We assume that this difference in the characteristic sizes of nanostructures in melt-spun ribbons could give a significant difference in the TE performance of SPSed pellets.

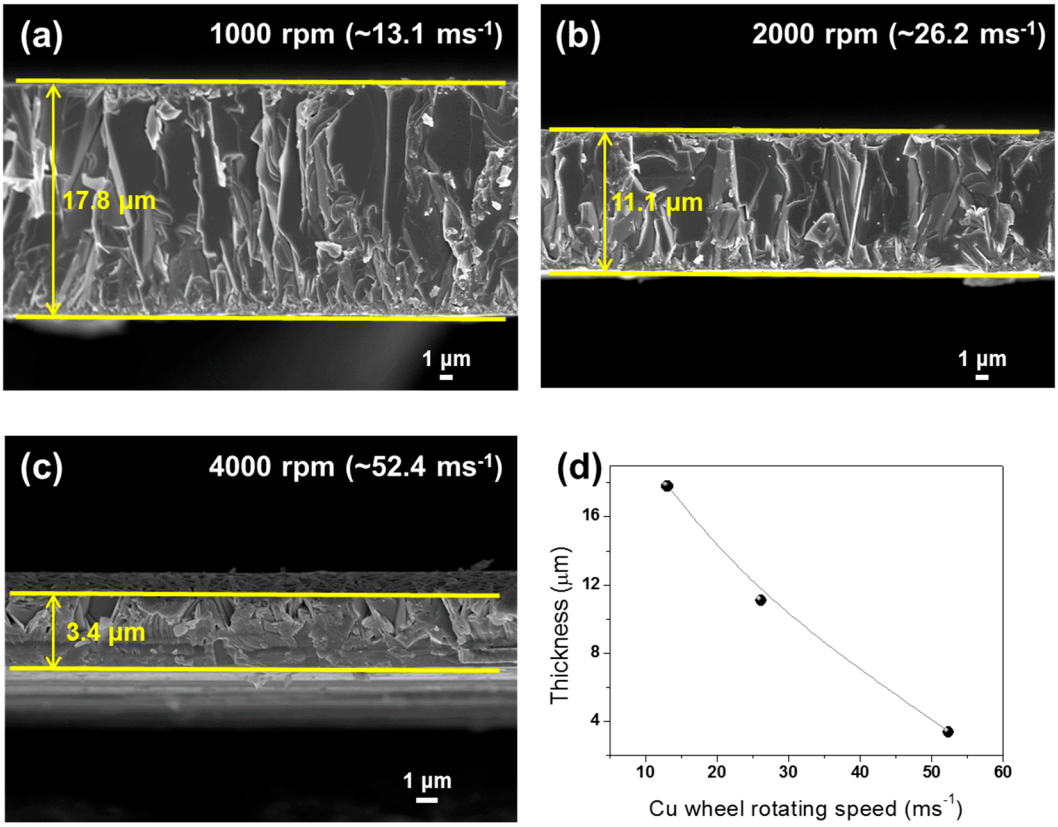

Figure 1. The cross-section SEM images of the melt-spun ribbons with varying Cu wheel rotation speed during melt spinning (MS) process. (**a**) 1000 rpm; (**b**) 2000 rpm; (**c**) 4000 rpm and (**d**) Plot of thickness with Cu wheel rotation speed (ms^{-1}).

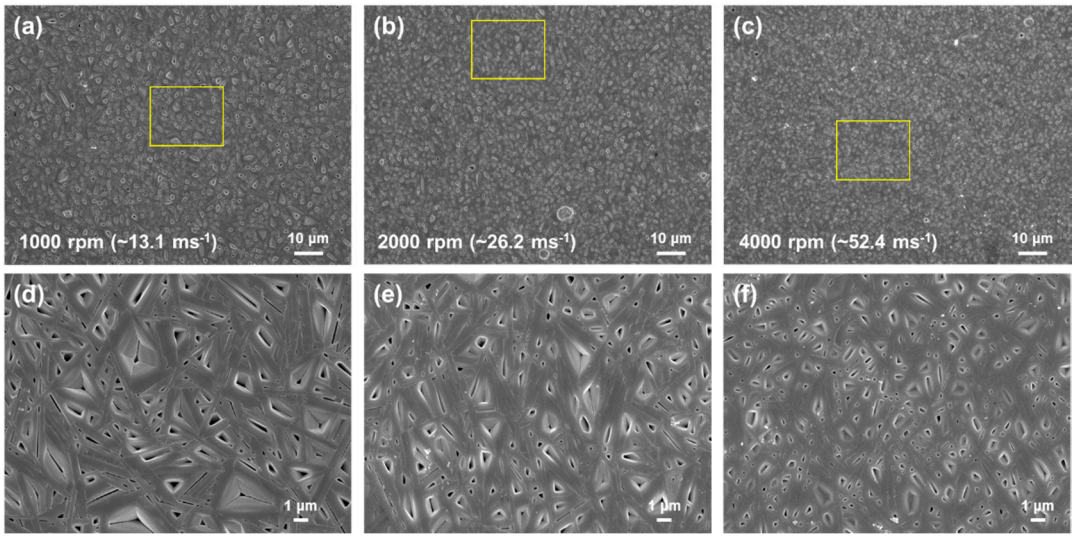

Figure 2. The SEM images of the free surfaces of ribbons with varying wheel rotation speed during the MS process: (**a**,**d**) 1000 rpm; (**b**,**e**) 2000 rpm; (**c**,**f**) 4000 rpm.

The melt-spun ribbons were ground into powders by using a mortar and sintered by using SPS technique. The relative densities of all the samples were >98%. Figure 3 shows the X-ray diffraction patterns of the SPSed pellets of $Bi_{0.36}Sb_{1.64}Te_3$ fabricated from melt-spun ribbons at 1000 (BST1000), 2000 (BST2000), and 4000 (BST4000) rpm wheel rotation speed. All samples show the fundamental diffraction peaks from Sb_2Te_3 with rhombohedral structure (JCPDS # 65-3678, R-3m space group). When the wheel speed was more than 2000 rpm, we can see an additional peak at $2\theta = 27.6^\circ$ corresponding to Te secondary phase (JCPDS # 36-1452). Meanwhile, the higher cooling rate led to the production of a larger amount of Te secondary phase, which can be easily found in Bi-Te-based TE materials [15]. There is no large difference of peak shift or peak intensity, which means that the structure of $Bi_{0.36}Sb_{1.64}Te_3$ is unchangeable with varying wheel rotation speed from 1000 rpm to 4000 rpm during the MS process. The fractured surfaces of the SPSed bulks are shown in Figure 4 to investigate the microstructure evolution during the SPS process. Interestingly, the grain size increased with increase of wheel rotation speed in the range of 1000 rpm to 4000 rpm. We assumed that the higher MS wheel rotation speed generates a smaller nanostructure of melt-spun ribbon, and thus the smaller nanograin structure can be maintained after the SPS process. However, our experimental results do not correspond with this assumption. As shown in Figure 4, the grain sizes of the SPSed pellets of BST1000, BST2000, and BST4000 are 17.9 μm, 19.4 μm, and 20.5 μm, respectively. It is noted that the grain sizes of SPSed pellets are much larger than the characteristic sizes of melt-spun ribbons. This phenomenon can be explained by the grain growth kinetics of nanoparticles. The smaller nanoparticles have lower melting point due to enhanced surface diffusion rate, leading to enlarged grain size [26]. Additionally, a larger amount of amorphous phase at higher wheel rotation speed can also be the origin of different grain size in the same sintering process [27]. This result suggests that a precisely controlled ultra-fast sintering process is required to obtain nanograin structured bulks from melt-spun ribbons.

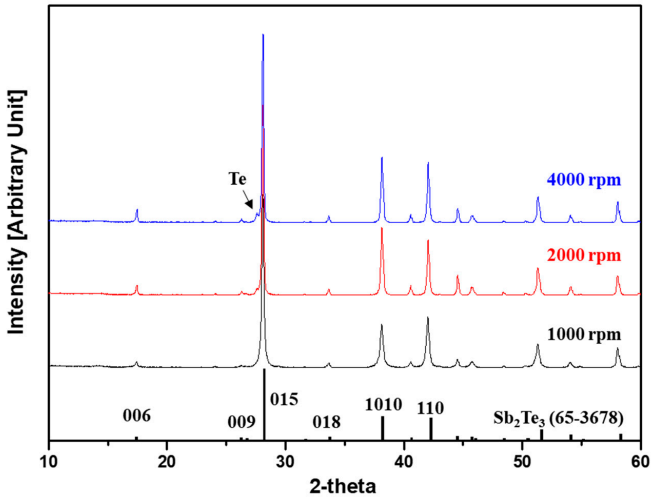

Figure 3. The XRD patterns of polycrystalline bulks of $Bi_{0.36}Sb_{1.64}Te_3$ fabricated from melt-spun ribbons at 1000, 2000, and 4000 rpm wheel rotation speed during the MS process. The bottom is the typical peak of Sb_2Te_3 (JCPDS # 65-3678).

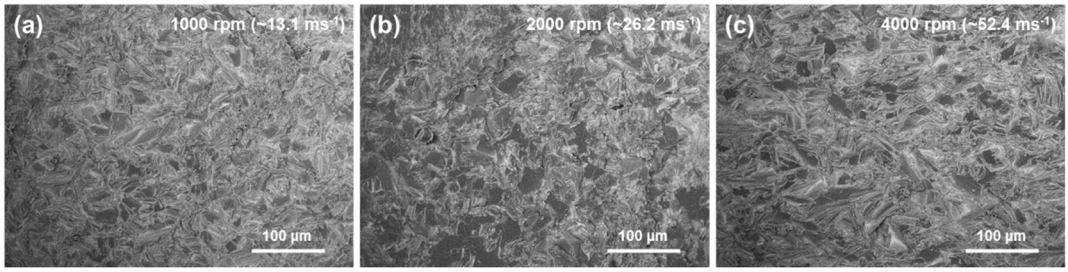

Figure 4. SEM images of fractured surfaces of the bulks of $Bi_{0.36}Sb_{1.64}Te_3$ fabricated from melt-spun ribbons at (**a**) 1000 (BST1000), (**b**) 2000 (BST2000), and (**c**) 4000 (BST4000) rpm wheel rotation speed during the MS process.

3.2. Thermoelectric Properties

Figure 5 shows temperature-dependent σ values for BST1000–BST4000 samples. All samples showed a decrease of σ with increasing temperature in the measured temperature range, indicating a metallic behavior. For BST1000, the room temperature σ value was 955 Scm^{-1}, while BST2000–BST4000 samples had similar room-temperature σ values of 1192 Scm^{-1}, 1201 Scm^{-1}, and 1163 Scm^{-1}, respectively. To clarify the electronic transport mechanism, the carrier concentration values of the samples were calculated by measuring Hall coefficient (R_H), as the following equation:

$$R_H = 1/pe \quad (1)$$

where p and e correspond to hole carrier concentration and electron charge, respectively. The carrier mobility (μ) is calculated by the following equation:

$$\sigma = pe\mu \quad (2)$$

Figure 5b depicts the room-temperature carrier concentration values for BST1000–BST4000 samples, which ranged from 2.87×10^{19} cm^{-3} to 3.86×10^{19} cm^{-3}. Interesting behavior was observed in the carrier mobility as shown in Figure 5c, in which the mobility increased from 191 $cm^2 \cdot V^{-1} \cdot s^{-1}$ to

254 $cm^2 \cdot V^{-1} \cdot s^{-1}$ with increase in the wheel rotation speed. This result is due to the reduced carrier scattering originating from the larger grain size at higher wheel rotation speed, as shown in Figure 4.

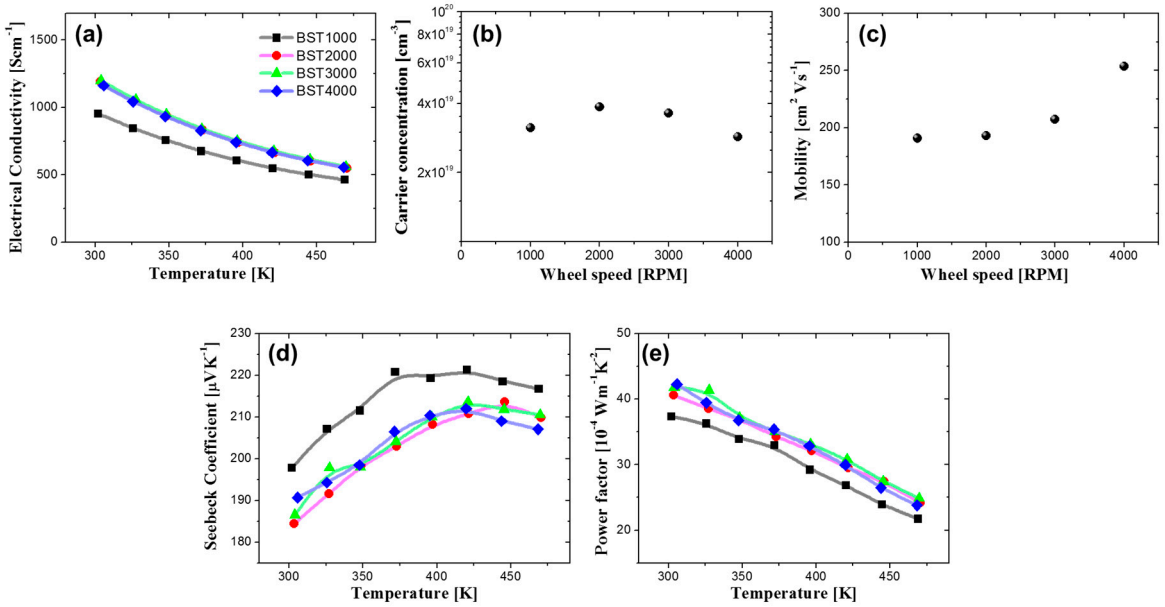

Figure 5. (**a**) Temperature dependence of electrical conductivity (σ); (**b**) carrier concentration and (**c**) mobility at room temperature; (**d**) temperature dependence of Seebeck coefficient (S); (**e**) temperature dependence of power factor (PF) for BST1000–BST4000 samples.

Figure 5d shows the temperature dependence of S for BST1000–BST4000 samples. The S values for all samples are positive, indicating that the major charge carrier is hole. The S increased with increasing temperature, reached a maximum at ~400 K, and decreased at high temperature, which is typical behavior presented in Bi_2Te_3-based TE materials mainly originating from the thermal excitation of minority carrier. The room temperature S values are 198 $\mu V \cdot K^{-1}$ for BST1000, 184 $\mu V \cdot K^{-1}$ for BST2000, 187 $\mu V \cdot K^{-1}$ for BST3000, and 191 $\mu V \cdot K^{-1}$ for BST4000, respectively. The S values of BST1000 showed the highest value within the measured temperature range due to the lower carrier concentration. Figure 5e shows the temperature dependences of PF values for BST1000–BST4000 samples. The PF value for BST1000 shows the lowest value of 37 $\times$ 10^{-4} $Wm^{-1} \cdot K^{-2}$ at room temperature due to the lowest σ, while the PF values of BST2000–BST4000 samples were almost the same over the whole measure temperature range (PF = 41–42 $\times$ 10^{-4} $Wm^{-1} \cdot K^{-2}$ at room temperature).

The temperature dependence of κ is displayed in Figure 6a. All samples showed similar temperature dependency of κ, where it decreased at low temperature and increased at high temperature, suggesting the effect of bipolar thermal conduction, while κ value increased with wheel rotation speed. To clarify this, we calculated the κ_{lat} value by subtraction of κ_{ele} from κ, in which κ_{ele} was estimated by the Wiedemann–Franz law ($\kappa_{ele} = L\sigma T$), using L = 2.0 $\times$ 10^{-8} $V^2 \cdot K^{-2}$ for degenerated semiconductor [28,29]. The κ_{lat} calculated from the above equations is shown in Figure 6b. The κ_{lat} of BST4000 was >10% higher than those of other samples, and κ_{lat} of BST2000 showed the lowest value within whole measured temperature range. These results fit well with the grain size variation against wheel rotation speed, which was already described by the microstructure of SPSed bulks. The largest grain size of BST4000 led to a reduction in the grain boundary phonon scattering, resulting in increased κ_{lat}.

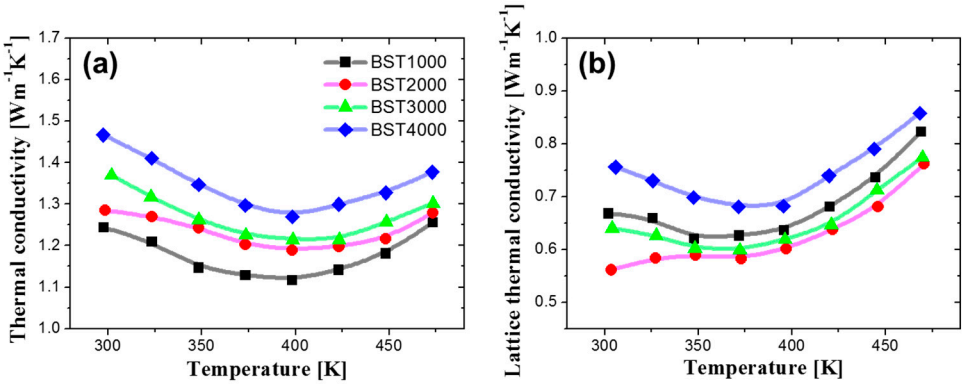

Figure 6. Temperature dependence of (**a**) total thermal conductivity (κ), and (**b**) lattice thermal conductivity (κ_{lat}) for BST1000–BST4000 samples.

The dimensionless figure of merit (ZT) values as a function of temperature for BST1000–BST4000 samples are shown in Figure 7. The ZT value increased with the temperature, and after a maximum near 400 K, it decreased at higher temperatures. The overall ZT values did not change significantly with the wheel rotation speed within the instrumental error range (~12%); the maximum ZT values were ~1.08 @ 370 K for BST1000, ~1.07 @ 400 K for BST2000, ~1.09 @ 400 K for BST3000, and ~1.02 @ 400 K for BST4000, respectively. Interestingly, BST4000 showed the lowest ZT_{max} compared to other SPSed bulk samples (BST1000–BST3000) despite the smallest characteristic size of its melt-spun ribbon (Figure 2). This is considered to be related to the microstructural evolution during the sintering process. As shown in Figure 2, the higher wheel rotation speed resulted in the smaller characteristic nanostructure size in melt-spun ribbons; however, the nano-scale grain structure could not be maintained in SPSed bulks due to the rapid grain growth during the SPS process, and grain growth was more prominent for BST4000. Therefore, some other fast sintering approaches to maintaining the nanostructure in melt-spun ribbon are highly required for boosting the grain boundary phonon scattering and ZT value.

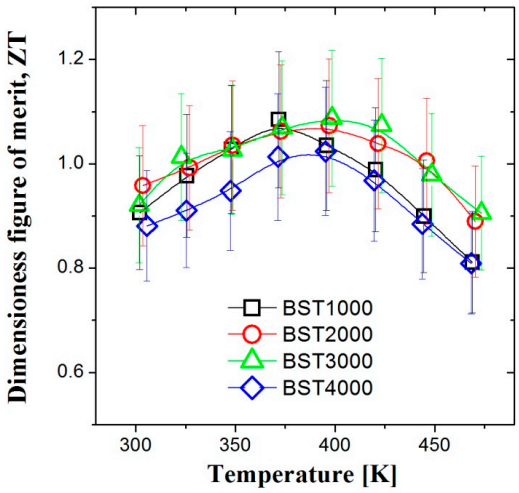

Figure 7. Temperature dependence of the dimensionless figure of merit (ZT) for BST1000–BST4000 samples.

4. Conclusions

We have synthesized polycrystalline bulks of $Bi_{0.36}Sb_{1.64}Te_3$ using melt spinning and spark plasma sintering processes. We varied the wheel rotation speed between 1000 rpm and 4000 rpm during the MS process, and the microstructures of the melt spun ribbons and sintered pellets were investigated. The thickness of the ribbon and the characteristic size of nanostructure on the free surface were reduced

as the wheel rotation speed increased due to higher cooling rate, while the grain size after spark plasma sintering significantly increased in value of ~20 μm for all SPSed bulk samples due to the rapid grain growth. The *ZT* values of BST1000–BST4000 did not change significantly with Cu wheel rotation speed, suggesting that small nanostructure size in precursors is not always preferable to enhance the thermoelectric performance of Bi_2Te_3-based TE materials in melt spinning process.

Acknowledgments: This work was supported by Dual Use Technology Program (12-DU-MP-01) of Agency for Defense Development, Republic of Korea, and also supported by a National Research Foundation of Korea (NRF) grant funded by the Korean Government (MSIP) (NRF-2015R1A5A1036133).

Author Contributions: W.H.S. and K.H.L. conceived and designed the experiments; J.S.Y., J.M., and J.M.S. performed the experiments; S.K. and R.J.W. analyzed the data; S.L. and W.S.S. contributed reagents/materials/analysis tools; W.H.S., S.W.K., and K.H.L. wrote the paper. All the authors contributed to the experiments, the analysis of the data, and edition of the manuscript.

Conflicts of Interest: The authors declare no conflict of interest.

References

1. Snyder, G.J.; Toberer, E.S. Complex thermoelectric materials. *Nat. Mater.* **2008**, *7*, 105–114. [CrossRef] [PubMed]
2. Bell, L.E. Cooling, heating, generating power, and recovering waste heat with thermoelectric systems. *Science* **2008**, *321*, 1457–1461. [CrossRef] [PubMed]
3. DiSalvo, F.J. Thermoelectric cooling and power generation. *Science* **1999**, *285*, 703–706. [CrossRef] [PubMed]
4. Heremans, J.P.; Jovovic, V.; Toberer, E.S.; Saramat, A.; Kurosaki, K.; Charoenphakdee, A.; Yamanaka, S.; Snyder, G.J. Enhancement of thermoelectric efficiency in pbte by distortion of the electronic density of states. *Science* **2008**, *321*, 554–557. [CrossRef] [PubMed]
5. Goldsmid, H. Bismuth telluride and its alloys as materials for thermoelectric generation. *Materials* **2014**, *7*, 2577–2592. [CrossRef]
6. Lee, K.H.; Kim, S.W. Design and preparation of high-performance bulk thermoelectric materials with defect structures. *J. Korean Ceram. Soc.* **2017**, *54*, 75–85. [CrossRef]
7. Wood, C. Materials for thermoelectric energy conversion. *Rep. Prog. Phys.* **1988**, *51*, 459. [CrossRef]
8. Kim, S.I.; Lee, K.H.; Mun, H.A.; Kim, H.S.; Hwang, S.W.; Roh, J.W.; Yang, D.J.; Shin, W.H.; Li, X.S.; Lee, Y.H. Dense dislocation arrays embedded in grain boundaries for high-performance bulk thermoelectrics. *Science* **2015**, *348*, 109–114. [CrossRef] [PubMed]
9. Kim, H.-S.; Gibbs, Z.M.; Tang, Y.; Wang, H.; Snyder, G.J. Characterization of lorenz number with seebeck coefficient measurement. *APL Mater.* **2015**, *3*, 041506. [CrossRef]
10. Kim, W.; Zide, J.; Gossard, A.; Klenov, D.; Stemmer, S.; Shakouri, A.; Majumdar, A. Thermal conductivity reduction and thermoelectric figure of merit increase by embedding nanoparticles in crystalline semiconductors. *Phys. Rev. Lett.* **2006**, *96*, 045901. [CrossRef] [PubMed]
11. Poudel, B.; Hao, Q.; Ma, Y.; Lan, Y.; Minnich, A.; Yu, B.; Yan, X.; Wang, D.; Muto, A.; Vashaee, D. High-thermoelectric performance of nanostructured bismuth antimony telluride bulk alloys. *Science* **2008**, *320*, 634–638. [CrossRef] [PubMed]
12. Tan, G.; Shi, F.; Hao, S.; Zhao, L.-D.; Chi, H.; Zhang, X.; Uher, C.; Wolverton, C.; Dravid, V.P.; Kanatzidis, M.G. Non-equilibrium processing leads to record high thermoelectric figure of merit in PbTe-SrTe. *Nat. Commun.* **2016**, *7*, 12167. [CrossRef] [PubMed]
13. Zhao, L.-D.; Lo, S.-H.; Zhang, Y.; Sun, H.; Tan, G.; Uher, C.; Wolverton, C.; Dravid, V.P.; Kanatzidis, M.G. Ultralow thermal conductivity and high thermoelectric figure of merit in snse crystals. *Nature* **2014**, *508*, 373–377. [CrossRef] [PubMed]
14. Rhyee, J.-S.; Lee, K.H.; Lee, S.M.; Cho, E.; Kim, S.I.; Lee, E.; Kwon, Y.S.; Shim, J.H.; Kotliar, G. Peierls distortion as a route to high thermoelectric performance in $In_4Se_{3-\delta}$ crystals. *Nature* **2009**, *459*, 965–968. [CrossRef] [PubMed]
15. Lan, Y.; Poudel, B.; Ma, Y.; Wang, D.; Dresselhaus, M.S.; Chen, G.; Ren, Z. Structure study of bulk nanograined thermoelectric bismuth antimony telluride. *Nano Lett.* **2009**, *9*, 1419–1422. [CrossRef] [PubMed]

16. Ma, Y.; Hao, Q.; Poudel, B.; Lan, Y.; Yu, B.; Wang, D.; Chen, G.; Ren, Z. Enhanced thermoelectric figure-of-merit in p-type nanostructured bismuth antimony tellurium alloys made from elemental chunks. *Nano Lett.* **2008**, *8*, 2580–2584. [CrossRef] [PubMed]
17. Nguyen, P.K.; Lee, K.H.; Moon, J.; Kim, S.I.; Ahn, K.A.; Chen, L.H.; Lee, S.M.; Chen, R.K.; Jin, S.; Berkowitz, A.E. Spark erosion: A high production rate method for producing $Bi_{0.5}Sb_{1.5}Te_3$ nanoparticles with enhanced thermoelectric performance. *Nanotechnology* **2012**, *23*, 415604. [CrossRef] [PubMed]
18. Cai, X.; Fan, X.A.; Rong, Z.; Yang, F.; Gan, Z.; Li, G. Improved thermoelectric properties of $Bi_2Te_{3-x}Se_x$ alloys by melt spinning and resistance pressing sintering. *J. Phys. D Appl. Phys.* **2014**, *47*, 115101. [CrossRef]
19. Ebling, D.G.; Jacquot, A.; Jägle, M.; Böttner, H.; Kühn, U.; Kirste, L. Structure and thermoelectric properties of nanocomposite bismuth telluride prepared by melt spinning or by partially alloying with IV–VI compounds. *Phys. Status Solidi RRL* **2007**, *1*, 238–240. [CrossRef]
20. Xie, W.; He, J.; Kang, H.J.; Tang, X.; Zhu, S.; Laver, M.; Wang, S.; Copley, J.R.; Brown, C.M.; Zhang, Q. Identifying the specific nanostructures responsible for the high thermoelectric performance of $(Bi,Sb)_2Te_3$ nanocomposites. *Nano Lett.* **2010**, *10*, 3283–3289. [CrossRef] [PubMed]
21. Min, Y.; Park, G.; Kim, B.; Giri, A.; Zeng, J.; Roh, J.W.; Kim, S.I.; Lee, K.H.; Jeong, U. Synthesis of multishell nanoplates by consecutive epitaxial growth of Bi_2Se_3 and Bi_2Te_3 nanoplates and enhanced thermoelectric properties. *ACS Nano* **2015**, *9*, 6843–6853. [CrossRef] [PubMed]
22. Min, Y.; Roh, J.W.; Yang, H.; Park, M.; Kim, S.I.; Hwang, S.; Lee, S.M.; Lee, K.H.; Jeong, U. Surfactant-free scalable synthesis of Bi_2Te_3 and Bi_2Se_3 nanoflakes and enhanced thermoelectric properties of their nanocomposites. *Adv. Mater.* **2013**, *25*, 1425–1429. [CrossRef] [PubMed]
23. Mehta, R.J.; Zhang, Y.; Karthik, C.; Singh, B.; Siegel, R.W.; Borca-Tasciuc, T.; Ramanath, G. A new class of doped nanobulk high-figure-of-merit thermoelectrics by scalable bottom-up assembly. *Nat. Mater.* **2012**, *11*, 233–240. [CrossRef] [PubMed]
24. Gheiratmand, T.; Hosseini, H.R.M.; Davami, P.; Ostadhossein, F.; Song, M.; Gjoka, M. On the effect of cooling rate during melt spinning of finemet ribbons. *Nanoscale* **2013**, *5*, 7520–7527. [CrossRef] [PubMed]
25. Tkatch, V.I.; Limanovskii, A.I.; Denisenko, S.N.; Rassolov, S.G. The effect of the melt-spinning processing parameters on the rate of cooling. *Mater. Sci. Eng. A* **2002**, *323*, 91–96. [CrossRef]
26. Jiang, H.; Moon, K.-S.; Dong, H.; Hua, F.; Wong, C.P. Size-dependent melting properties of tin nanoparticles. *Chem. Phys. Lett.* **2006**, *429*, 492–496. [CrossRef]
27. Donovan, E.; Spaepen, F.; Turnbull, D.; Poate, J.; Jacobson, D. Heat of crystallization and melting point of amorphous silicon. *Appl. Phys. Lett.* **1983**, *42*, 698–700. [CrossRef]
28. Xu, Z.J.; Hu, L.P.; Ying, P.J.; Zhao, X.B.; Zhu, T.J. Enhanced thermoelectric and mechanical properties of zone melted p-type $(Bi,Sb)_2Te_3$ thermoelectric materials by hot deformation. *Acta Mater.* **2015**, *84*, 385–392. [CrossRef]
29. Xie, W.; Tang, X.; Yan, Y.; Zhang, Q.; Tritt, T.M. Unique nanostructures and enhanced thermoelectric performance of melt-spun BiSbTe alloys. *Appl. Phys. Lett.* **2009**, *94*, 102111. [CrossRef]